



Maine Space Grant Consortium  
Maine Aerospace Workforce Development Program

Student Research Experiences at NASA Field Centers  
Summer 2005

87 Winthrop St., Suite 200  
Augusta, ME 04330  
877-397-7223  
(207)622-4548-fax  
[www.msgc.org](http://www.msgc.org)  
[info@msgc.org](mailto:info@msgc.org)

**Letter from the Executive Director**  
**Dr. Terry Shehata**

The Maine Space Grant Consortium (MSGC) is pleased to distribute the results from the third year of its “Maine Aerospace Workforce Development Program”. The “Student Research Experiences at NASA Field Centers for the summer of 2005” is a compilation of extended abstracts from seven undergraduate students participating in a 10-week research project at a NASA field center.

Our goal in the program is to motivate outstanding undergraduates in Maine to seriously consider career opportunities related to aerospace research and education.

This program is supported with Workforce Development funds from NASA’s National Space Grant College and Fellowship Program and provides undergraduate students attending Maine colleges and universities, who are interested in pursuing careers vital to the nation’s aerospace-related industrial complex, with a 10-week productive research experience at NASA field centers.

The program’s third year resulted in 19 student responses, eight submitted applications and seven awards to six different NASA field centers. Upon their return to Maine, each student was required to present to at least two different high schools in Maine to inspire students to continue into higher education in the fields of space and space-related sciences. In addition, students were required to present to an MSGC board and affiliate member meeting.

Each student is tracked academically and professionally for five years from the date of the award, to evaluate the success of the program and to monitor further participation in research programs, accomplishments in referring journal articles for publication, presenting at conferences, and submitting proposals.

MSGC distributed a survey to each student and mentor at the end of the summer and found from the data collected and the comments made by both students and NASA mentors, that this program was truly a success. See below for comments:

“The whole experience was unbelievable! I feel grateful to have had the opportunity. It allowed me to gain a more clear understanding of my research interests and possibilities for future research. I went into this internship with a general idea of what I was interested in, and came out with a clear objective for future graduate work” – Heather Throckmorton, University of Southern Maine student, participated at the Goddard Space Flight Center

“Keep up the good work recruiting superior individuals such as Amanda Hoover” – Mark Strickland, Marshall Space Flight Center

“This (MSGC’s Aerospace Workforce Development Program) is an excellent program that benefits both the students and NASA research teams. I hope that NASA will continue to fund, and even expand, programs such as this” – Dr. Charles Meegan, Marshall Space Flight Center

DISCLAIMER:

This document was prepared as an account of the work sponsored by the NASA field centers and the Maine Space Grant Consortium (MSGC). Neither the NASA Field centers or MSGC, nor any of their employees makes any warranty, implies, or assumes any legal liability or responsibility for the accuracy or completeness of any information. The student technical reports are the original technical reports submitted by the student participants. No changes have been made by MSGC.

The use of trade names of manufacturers in this report does not constitute an official endorsement of such products or manufacturers, either expressed or implied, by the National Aeronautics and Space Administration.

Kristy Albee  
University of Maine

Participating at the Marshall Space Flight Center

Title: "GLAST"

NASA Mentor Dr. Charles Meegan



It is planned for the fall of 2007 that the telescope GLAST (Gamma-Ray Large Area Telescope) will be launched and the mysterious realms of gamma-rays can once again be studied extensively. While working at NSSTC (National Space Science and Technology Center) for ten weeks, much has been learned about GLAST and its components, specifically the GBM project and team. GLAST, which will detect and measure gamma-rays, is quite a unique and fascinating spacecraft made up of two distinct components: LAT (Large Area Telescope), and GBM (GLAST Burst Monitor). While at NSSTC, I have retained knowledge about GLAST, gamma-rays and the history of their existence, the components of GLAST (specifically GBM), how gamma-rays will be detected, and in the areas of personal work such as LabVIEW, html, Excel, and various other jobs.

GLAST will be flown in low-Earth orbit and will operate in both the zenith pointing mode and stare mode. At one point in time, GLAST will be able to view more than 16 percent of the sky. While in the zenith mode, with every orbit it will view approximately 75 percent of the sky. It will detect gamma ray energy from 20 million to greater than 300 billion electron volts (the energy of visible light is about 2 electron volts), an incredible amount of sensitivity.<sup>1</sup>

While knowing all this information about GLAST is all well and good, but its primary function, to detect and measure gamma-rays, knowledge of what is a gamma-ray is of a necessity. Gamma-rays are a form of energy that have the smallest wavelengths and the most energy of any other wave in the electromagnetic spectrum. They are the most energetic form of light, (gamma-rays are millions to billions of times more energetic than visible light) and are generated by radioactive atoms and in nuclear explosions. GRB 970508 created the same energy in 15 seconds as the sun would in 10 billion years. Such gamma-ray sources include ancient black holes, matter-antimatter annihilation, spinning neutron stars, immense solar flares, and colossal star explosions. In learning about these, in future we may be able to “reveal secrets about the structure and evolution of the Universe”.<sup>4</sup>

As mentioned told above, GLAST will consist of two instruments to observe these highly active gamma-rays: the LAT (Large Area Telescope) and GBM (GLAST Burst Monitor). The LAT, which is being constructed at Goddard Space Flight Center, will detect and measure the higher intense gamma-rays with an energy range approximately 20 MeV through 300 GeV ( $1\text{eV} = 1.6 \times 10^{-19} \text{ J}$ ).<sup>2</sup> (Other affiliations and information on the LAT can be found at <http://glast.gsfc.nasa.gov/science/instruments/> and <http://www-glast.stanford.edu/>).

A team at Marshall Space Flight Center in Huntsville, Alabama and MPE (Max Planck for Extraterrestrial Physics) in Garching, Germany is constructing the GBM project. The Marshall team is in charge of all the programming, setup, cabling, and all the tests and procedures needed to make the project flight ready as well and integrating the detectors in with their work. MPE is primarily in charge of the development of the detectors and the power supplies. GBM will consist of two types of detectors: twelve NaI detectors and two BGO detectors. (The BGO detectors are pretty much two NaI detectors butted together but with a slightly different make up.) These detectors will pick up gamma-rays

that are lower in energy. The NaI detectors' energy range is between 5 KeV and 1 MeV, and the BGO's energy range is 150 KeV to 30 MeV. There is some overlap with the detectors and with the LAT which could result a much more dynamic investigation.<sup>2</sup>

So how do the detectors work? Tracing a gamma-ray photon from some source it travels through the Universe largely unobstructed and comes into contact with, say, the plate of a NaI detector. (There are twelve of them pointed in different regions therefore a gamma-ray photon is surely to hit one (or more) of the detectors). The photon hits the plate and enters a crystal (about 2/3 thick) of sodium iodide (used because of high atomic number) where the energy is absorbed and transferred to light. This optical light photon then proceeds out of the crystal further into the detector until it reaches a photomultiplier lens. As the photon continues further in the photomultiplier tube, a current of voltage is created and is picked up by the DPU (Data Processing Unit) where it is recorded and stored, sending back to earth this increase of voltage. A gamma-ray photon cannot be directly seen, therefore, changing the form of energy allows us to indirectly "see" it and measure it.<sup>5</sup>

The Marshall team and MPE, through telecom, collaborate regularly as things progress. At least every other Wednesday there is a meeting where action plans, near-term milestones, schedules, and any problems or obstacles relevant are discussed. Communication flows well between the two countries as well as throughout the group. Trips are planned between Garching, Germany and Huntsville, Alabama as time allows. During my stay I was pleased to personally meet three men from MPE as they visited our lab to see how everything was coming along and to partake in a yearly science team meeting.

My ten weeks working with this group has introduced me up to many windows of opportunity. My work at the NSSTC with the GBM team included learning a few programs, procedures, and tests. Learning LabVIEW, a computer program that uses icons instead of lines of text to create application became the prominent goal of the ten-week stay. As opposed to instructions determining program execution as in a text-based programming language, LabVIEW uses dataflow programming; execution is determined by the flow of data.<sup>3</sup> In LabVIEW, displays were made for the Telemetry Database. I worked on eight of such displays: Telecommand Log, FSW Error Log, PSB Status, Boot, Configuration & Status, Analog, Telecommand Verifiers, PHA Configuration, and Detector Rate.

I also learned how to create a web page in HTML through updating the NSSTC Gamma-Ray Astrophysical team's publication web page. Approximately 500 files of publications from January 2001 to July 2005 were reviewed. In the end (after omitting replications due to collaborations and those not in the group) 100 publications were added to the web page. This can be viewed at <http://gammaray.nsstc.nasa.gov/publications/>.

Becoming more familiar with Excel was also present. Graphs and charts were required to be made of the correlation between temperature and resistance of a certain thermocouple. From the graph an equation was obtained to best model the behavior of this correlation.

I also became familiar with and built many cables. I also became familiar with testing those cables for grounding and pin placement. They possessed some “problem” cables that were fixed by ground testing and checking pin placement. These tests were done as well to working cables to be sure not to damage any of the flight hardware (DPU, cables, and detectors).

Detector mounts were made by one of the team members to hold the flight detectors in during testing. I then took on the responsibility of putting the mounts together once the pieces were made and anodized. Other various jobs included drilling holes in a metal container to make a power box, dry-run test procedures, and gaining as much information about gamma-rays as I could.

This internship was quite insightful and I feel quite lucky to have been part of it. I have had the chance to work with amazing and inspirational people who have shown me many of the possibilities NASA has to offer. I know this experience will have positive, lasting effects on me as I continue on in school and find the best career suited for me. I am grateful for this chance and hope that I will have many more like it in the upcoming years; I have much to look forward to.

### Sources of Reference

<sup>1</sup>GLAST: Gamma-ray Large Area Space Telescope. 2005. <<http://glast.gsfc.nasa.gov/>>. (in form of brochure)

<sup>2</sup>GLAST: Exploring the High Energy Universe. Lynn Cominsky (Sonoma State University & NASA's GLAST Mission, California) and Christopher Wanjek (NASA/GSFC, Maryland).

<sup>3</sup>National Instruments. LabVIEW 7 Express: User Manual. Austin, Texas: National Instruments Corporation, 2003.

<sup>4</sup>Schilling, Govert. The Hunt for the Biggest Explosions in the Universe. Cambridge, UK: Cambridge University Press, 2002.

<sup>5</sup>Dr. Charles Meegan (NASA/MSFC) PI of GBM

### Sources of Interest

Katz, Jonathan I. The Mystery of Gamma-Ray Bursts: The Most Violent Explosions in the Universe. New York: Oxford University Press, 2002.

Kitchin, C. R. Astrophysical Techniques. Bristol: Adam Hilger Ltd. 1984.

A Brief History of Gamma-ray Astronomy. Gordon Spear. GTN (Global Telescope Network). 30 June 2005  
<<http://gtn.sonoma.edu/public/resources/history/index.php>>.

Gamma-Rays. Goddard Space Flight Center, NASA. 7 June 2005  
<<http://imagers.gsfc.nasa.gov/ems/gamma.html>>.

Gamma-Ray Burst Physics. Nikos Drakos. 26 January 1994. University of Leeds. 9 June 2005 <<http://www.astro.psu.edu/users/nnp/grbphys.html>>.

The History of Gamma-Ray Astronomy. Dr. Nicholas White. 1997-2005. Goddard Space Flight Center, NASA. 7 June 2005  
<[http://imagine.gsfc.nasa.gov/docs/science/know\\_11/history\\_gamma.html](http://imagine.gsfc.nasa.gov/docs/science/know_11/history_gamma.html)>.

Samuel Frankel  
University of Southern Maine

Participating at the Ames Research Center

**Title:** “Characterization of A Mouse Model For Altered Integrin  
Function In Bone”

NASA Mentor Dr. Ruth K. Globus



One of the challenges facing astronauts is the effect of a weightless environment on the physiology of the skeletal system. Bone development and remodeling processes are influenced by mechanically-induced cellular signaling. But microgravity alters the environment of mechanical pressures that are required for normal, terrestrial homeostasis. As such, systems of skeletal maintenance are compromised in a weightless environment.

The specific mechanisms that translate mechanical information, such as the pressure of gravity, into a biological response are unknown. Cell culture experiments suggest that mechanical stimuli are transmitted by a specific form of integrin receptor on a type of bone cell called osteoblasts. These cells are located on the outer surface of bones and act to produce new tissue, both during initial bone growth and to balance the activity of bone destroying osteoclasts during the normal remodeling process. Integrins are a class of transmembrane receptors that mediate the cell's adherence to extra-cellular matrix (ECM) proteins. ECM is connective tissue that surrounds and supports cells. It is theorized that the pressures of mechanical stimulus are translated into biological information through ECM interaction with  $\beta 1$ -integrin receptors of osteoblast cells.

Integrin receptors are heterodimers with  $\alpha$  and  $\beta$  subunits, bridging the osteoblast cell membrane. Different combinations of  $\alpha$  and  $\beta$  subunits form functionally distinct types of integrins, of which more than twenty have been identified. The term " $\beta 1$ -integrin" refers to an integrin receptor containing the  $\beta 1$  subunit paired with one of several complementary  $\alpha$  subunits. How  $\beta 1$ -integrins influence bone homeostasis *in vivo* and biological reaction to mechanical stimuli are major questions in cell biology.

In order to study the function of  $\beta 1$ -integrins, the lab maintains a transgenic mouse line with a conditional knockout of the  $\beta 1$ -subunit specific to osteoblasts. These mice continue to have integrin receptors, but only those combinations of  $\alpha$  and  $\beta$  subunits that do not include  $\beta 1$ . This is significant because  $\beta 1$ -integrins are functionally distinct in their ability to bind an important ECM-protein called collagen. The various types of integrins are often redundant in their ability to bind ECM-proteins. However, according to current understanding of integrin function, deletion of the  $\beta 1$  subunit eliminates all the combinations able to bind collagen.

The most ever-present mechanical stimulus on terrestrial organisms is gravity. However, in a weightless environment, vertebrates experience significant loss of bone mass over time. This implies that the cell signaling system guiding bone maintenance, of which  $\beta 1$ -integrins are suspected to be integral components, is affected by the lack of gravitational pressure. In order to characterize the function of  $\beta 1$ -integrins, differences between  $\beta 1$ -deleted and control mice were examined after use of the hindlimb-unloading procedure. Hindlimb unloading, a well established model of microgravity, removes mechanical stimuli from the rear limbs.

Mice were placed in a harness that suspended their rear limbs from the ground. The harness distributed the animal's weight so as to avoid causing pain. Although restricted to use of their front limbs, the mice were able to move around the cage and had free access

to food and water. While unloaded, the health of the mice was monitored by tracking weight and food intake. After seven days the mice were euthanized and dissected. Femora, tibia, and sections of spinal cord were cleaned and stored for morphometric and histological analysis. The thymus and adrenal glands were cleaned and weighed as a gross measure of stress. Collected tissues are to be analyzed upon reaching an appropriate sample size for each genotype.

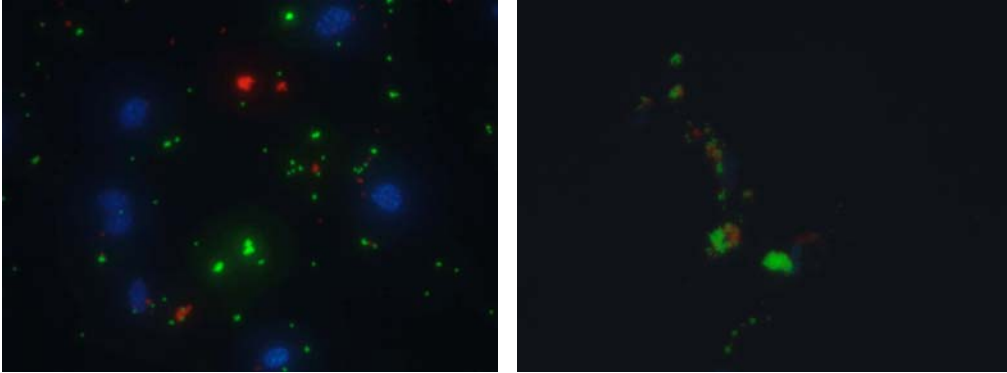
In addition to the cooperative hindlimb-unloading project, I worked individually to characterize the functional adherence of  $\beta 1$ -deleted osteoblasts. Although theoretically  $\beta 1$ -deleted osteoblasts should be much less able to bind collagen, it is important to determine their actual abilities. My aim was to refine an assay based on the binding of fluorescent “microspheres” to cells. Microspheres are beads made of fluorescent latex, available in different colors and sizes. They can be coated with an adhering substrate and used to mark different cellular characteristics. Multiple cell characteristics can be examined simultaneously using differently colored beads.

The targets of the assay were primary osteoblasts, dissociated and cultured directly from animal tissue. Femora and tibia were digested at length in order to break down the bone and release cells into solution. Isolated cells were cultured until reaching an appropriate density, and then incubated with microspheres overnight.

Green and red microspheres were coated with the ECM-proteins collagen and fibronectin (vitronectin in later experiments) respectively. Cells were incubated with equal concentrations of each type in order to compare the binding ratio. Microspheres adhered to the cells when ECM-proteins found appropriate receptors on the osteoblast cell membrane. Because all the forms of integrin receptor that bind collagen contain the  $\beta 1$ -subunit, the relative binding ratio of collagen to other ECM-coatings may be altered in  $\beta 1$ -deleted cells. The cells were imaged under a fluorescent microscope in order to determine the color ratios of successfully adhered microspheres. Over the summer I was able to develop, troubleshoot, and document the assay for future use.

Work conducted in the Bone & Signaling laboratory is aimed at mapping the molecular pathway that converts mechanical stimuli to biological information. Determining the molecular and functional significance of the components will lead to a greater understanding of bone development and maintenance. In addition to clinical relevance on Earth, this knowledge will provide the foundation to overcome one of the obstacles faced by astronauts venturing into space.

A comparison of unbound microspheres (left) and bound microspheres (right). Green spheres are coated with collagen, red spheres with fibronectin. Cell nuclei marked with a blue dye (unfortunately fainter in right hand image).

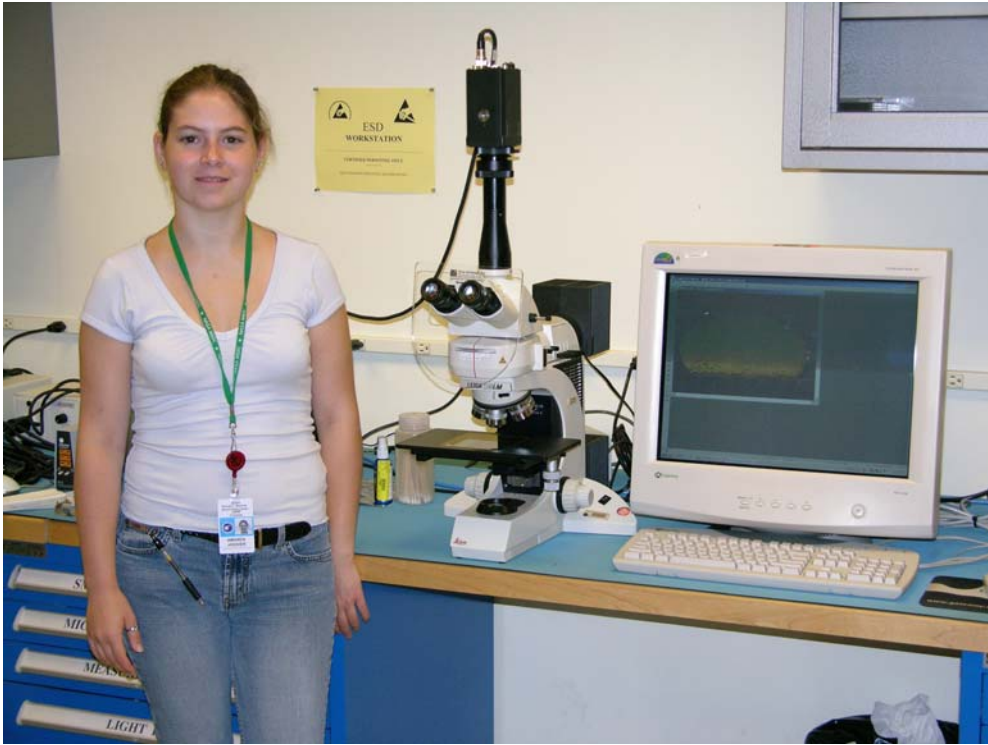


Amanda Hoover  
University of Maine

Participating at the Marshall Space Flight Center

Project title: “ Using Thermal Imaging to Detect Failed Solder  
Balls in Ball Grid Array Test Samples”

NASA Mentor Mark Strickland



## **Abstract:**

This report covers the examination of ball grid arrays (BGA) test samples using thermal imaging techniques and parts examination via cross-sectioning. The BGA's were daisy chained to a board and tested with a hot plate. The test consisted of taking data at ambient and hot temperatures. An infrared camera observed the board throughout the process of heating and cooling. Cross-sectioning was performed to confirm the failed solder balls and validate thermography results. The spots found with thermal imaging were marked on the chip and damaged solder balls were found in those spots during cross-sectioning. Thermal imaging proves itself as a good indicator of failed solder balls in the test discussed in this paper.



**PICTURE OF THERMAL IMAGING LAB ROOM**

## **Introduction:**

The technique used in this experiment was thermal imaging with an infrared camera (IR). The camera reveals higher resistance areas (hot spots also referred to as failures) on the board as current and voltage are applied. With the images, a solder ball is pin-pointed in most every case that a hot spot shows up. Without the IR camera, isolating the location of the failed solder ball joint would take a long time.

A total of 16 boards were tested beginning in the Summer of 2002 and testing continued until 2004. The boards are separated into four categories; solder paste/underfill, solder paste/non-underfill, SIPAD/underfill, and SIPAD/non-underfill. Each category has four boards associated with it. The board numbers that correspond to the categories above are SP1-4, SP5-8, S1-4, and S5-8, respectively. The boards were tested in a thermal chamber that cycled between  $-55^{\circ}\text{C}$  and  $100^{\circ}\text{C}$ . The cycles started at ambient temperature and

cooled slowly until  $-55^{\circ}\text{C}$ . Once at  $-55^{\circ}\text{C}$  the board soaked for 15 minutes and then slowly increased temperature until it reached  $100^{\circ}\text{C}$ , at which it soaked for 15 minutes. If a failure occurred, the failed boards were removed for thermal imaging and then returned for additional testing. The initial thermal imaging revealed hot spots that disappeared after the boards were exposed to additional thermal cycles. The majority of the boards remained in the chamber until exposed to 3026 cycles. Data was recorded electronically and the software recorded failed channels based on a preset resistance threshold of 1000 ohms. When a channel exceeded 1000 ohms at 10 different instances within a 10% cyclic window the software recorded a failure. In other words, if the first high resistance occurred at 100 thermal cycles then the next nine high resistance readings would have to occur prior to 110 thermal cycles.

The focus of this paper is testing that was performed in the Summer of 2005. The testing used BGA boards previously experimented with in the thermal chamber, but with a hot plate instead. Board SP1 is the testing sample and is discussed henceforth. This board has six BGA parts: two are BGA 169, two are BGA 225, and two are BGA 352. Both BGA 169 and BGA 225 are full array designs and BGA 352 is a perimeter array design. See **Figure 1** for pictures of the board.

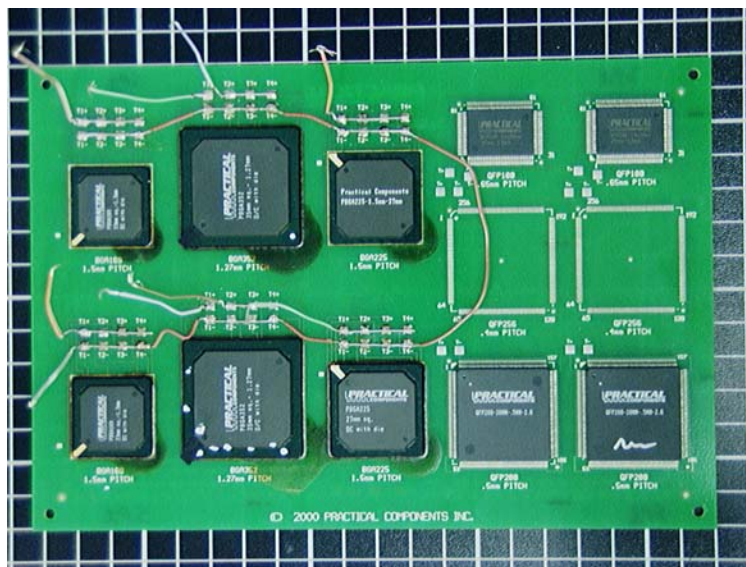


**Figure 1:** A picture of the board to see the layout of the chips. The largest chips are the perimeter arrays. Along with the layout of the chips, the hot spots observed during testing are marked. (More regarding hot spots in the experimental section)

### **Experimental:**

The SP1 board had failures in BGA chips 352-1 and 2. During thermal imaging the camera is focused on these two chips. Refer to **Figure 2** for location of the BGA 352's. The daisy chained solder balls were wired up into four channels between the two BGA

352 chips below. The channels monitored either the left quadrant or the remaining three quadrants depending on the wire that attached to the channel. The channels observed are 67, 68, 69, and 70, seen below.

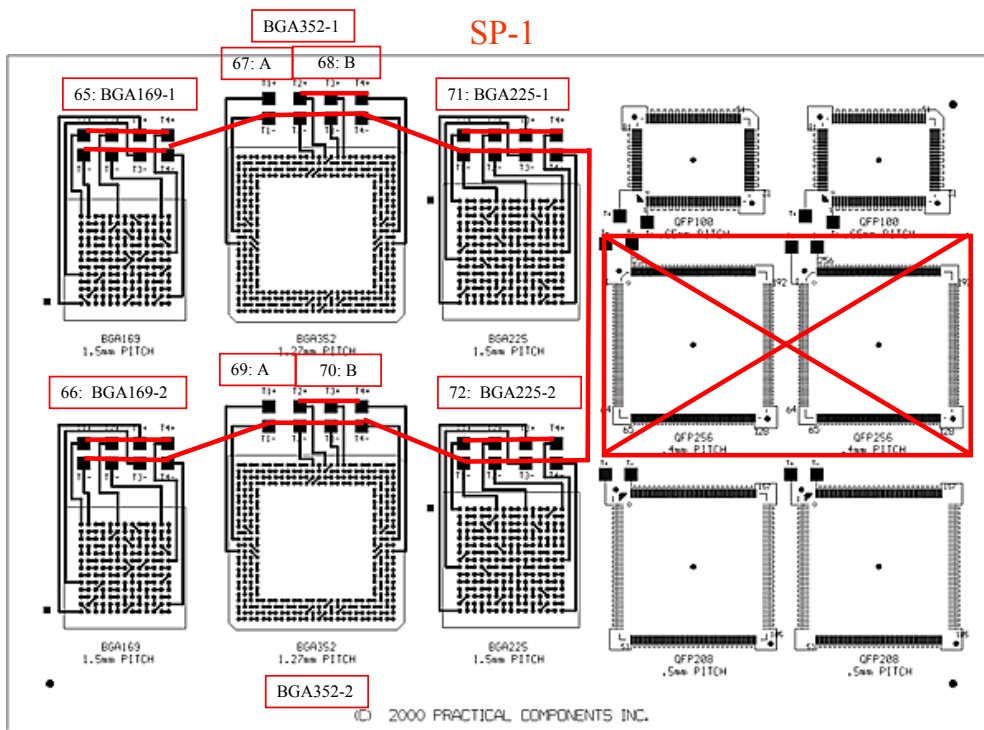


**FIGURE 2: A diagram of the SP-1 board. The bold lines are the outline of the wires and the Channels are labeled in boxes above the chip. Channels 67-70 are the only concern in this report.**

The first hot spot test was performed at 19°C , ambient temperature. The resistance was taken for a channel with an ohmmeter. The channel was clamped to the power supply and the supply was turned on. The power supply reported readings of current and voltage and also allowed for setting limitations. The voltage was set to 5 volts.

A hot plate was used to heat up the board. The hot plate temperature was set to 100°C . The camera focused on BGA chip 352-1 and the board was observed until it reached about 100°C . Resistance was recorded at 100°C . And then the board was allowed to cool down so the next channel could undergo the same process. The ambient temperature changed for each channel because all heat could not be lost unless a day's wait occurred. A new channel would begin the testing process once the temperature cooled to a range of 20°C to 23°C .

Cross-sectioning was the next step in proving the reliability of thermal imaging. Once the pictures from the IR camera were transferred and analyzed, the hot spots were marked on the chip where they appeared. **Figure 1** has the hot spot locations marked on it. The chips were removed from the board, keeping the solder joints intact, with a precision diamond saw. The original orientation of the channels was scribed on a paper diagram and on the chips. The next step to prepare for cross-sectioning is to pot the parts into an epoxy mixture. The mixture is prepared by combining 5 parts of Buehler Epoxicure Resin with 1 part Buehler Epoxicure Hardener. It takes 6 hours for complete curing. Once cured, the part is ready for grinding and polishing. Grinding is a four to five step process from post cure to grinding down to the desired surface. It is quicker to start with 60 grit pads until the chip is reached, then grind through 240 grit, 400 grit, 800 grit, and 1200 grit respectively. Polishing comes after the grinding process and is completed in two steps. First the epoxy covered chip goes through a rough diamond pad polish (6 microns diamond) and is then finished with a final alumina pad polish (0.05 microns alumina). After the row of balls are final polished, the row is observed under a microscope to inspect the condition of the solder balls. The grinding and polishing occur for each row twice; the perimeter array has four rows of solder balls. Two slices are taken to observe each section of the ball. The slices were either at the 1/3 mark, 1/2 mark, or the 2/3 mark. It is hard to judge the exact location, but two of the three marks were observed. When another slice on the part is taken, grinding can start at 400 grit and continue through the steps to final polish. Cross-sectioning of both the chips was taken on sides where the hot spots were marked. Etching was done to the row of solder balls when the balls appeared smudged through a microscope. A 2% Nital formula was used one time but it caused noticeable staining. Etching with this solution was carried out 2 times for 3 seconds each. The etch was prepared by combining 2mL of  $\text{HNO}_3$  and 98mL ethanol. Due to the level of staining another etching formula was used for subsequent rows. This etch was prepared by mixing 100mL  $\text{H}_2\text{O}$ , 10g  $\text{SnCl}_2$  and 5mL  $\text{HCl}$  and much better results were observed compared to the Nital etch. The formula was applied on the row for 6 seconds each time used.

### **Results and Discussion:**

The conditions the boards experienced in the thermal chamber are important in analyzing the data collected and the cross-section results. The boards were positioned in the chamber with the wires pointing to the back. Figure 1 can be referenced to see wires on board. The chamber is designed to circulate hot and cold air around to regulate the desired temperatures. The air blows from the back of the chamber. (See **Figure 3**.) The temperature in the chamber changes gradually. The soak times are the only times that the temperature stays constant. The soak temperatures are  $-55^\circ\text{C}$  and  $100^\circ\text{C}$ . Resistance magnitudes also help to predict if a failed solder ball will be present prior to thermal imaging.



**Figure 3: Image of Thermal Chamber. The boards slide in sideways  
And air blows at the boards from the back.**

The resistance magnitude will not show the location of the ball, in which case thermal imaging is introduced. A resistance magnitude greater than  $4k\Omega$  does not show images from the thermal camera. It has not yet been determined the maximum resistance reached before a prediction about a failed ball can happen. Resistance magnitudes between  $10\Omega$  and  $15\Omega$  have shown possible failures. Three of the four channels with resistances in that range, at hot or ambient temperatures, revealed hot spots. Thermal imaging showed us that different corners of the channels would heat up. It is not uncommon to see a channel closed at ambient temperature and open at a hotter temperature and vice versa. Pictures were taken of bright hot spots with the thermal camera.

When cross-sectioning the chips, the location of the failed balls was consistent with the thermal imaging results. Pictures of clear thermal images and the suspected failed solder balls that are associated with them are attached on back page. On BGA 352-1, a probe test was done to see if resistance was present in the individual balls. One of the balls was cracked open with a large gap and the other was cracked with hardly any separation. We found that the ball with the large gap had no current running through it, but the other ball had some. **Figure 4** compares the cracks of both balls next to each other.

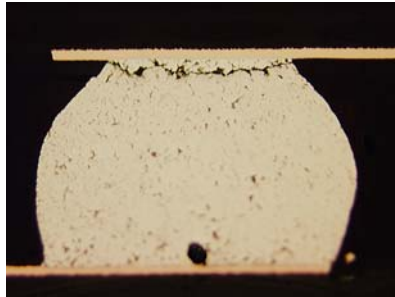


**Figure 4a: The solder ball with a large break along top. No current runs through this ball, which makes the channel appear dead. This is the second ball in the row.**

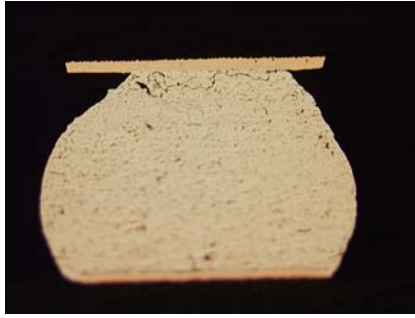


**Figure 4b: The solder ball with a small break along top. Some current runs through this ball but a small amount. The channel will have a hot spot appear because of the small connection. This is the last ball in the same row as 4a.**

Etching showed the origin and path the crack followed. The lead concentration vs. tin concentration in the solder ball was vivid after etching. Most times a separation will appear and travel along lead rich areas. The lead grains were more defined on the outer edge. This makes sense because the BGA is a perimeter array configuration. The outer rows experience more thermal stress due to differences in the rates of thermal expansion. The full array parts (BGA 225 and BGA 169) had no known failures from the thermal chamber tests and the hot plate. The underfill did not react well to the thermal testing. Cracks in the underfill between the solder balls were found. (See **Figure 5.**) The temperatures exceeded the comfort temperatures of the underfill. More tests will be done to examine this more closely.

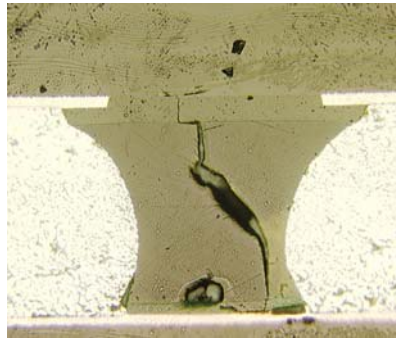


**Figure 5: A crack through the underfill and pushing through the chip at the top. Similar cracks were observed between other solder balls.**

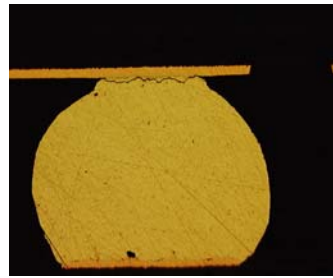
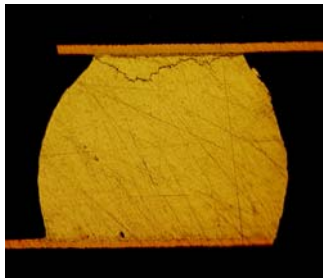
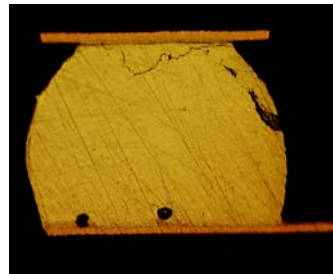
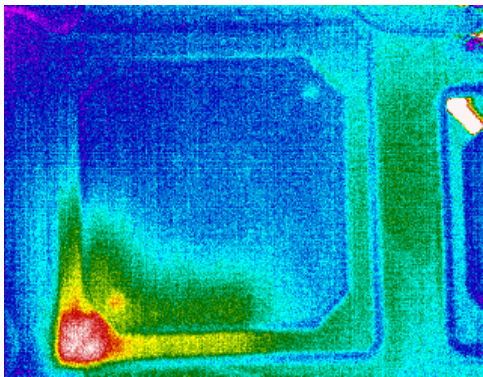
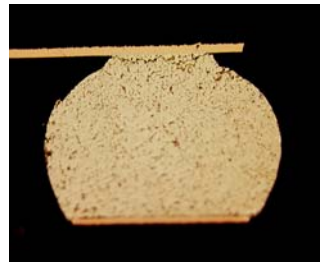
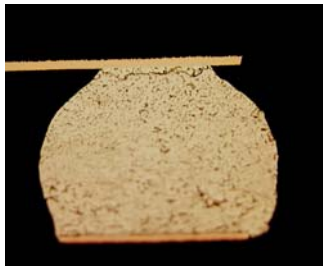
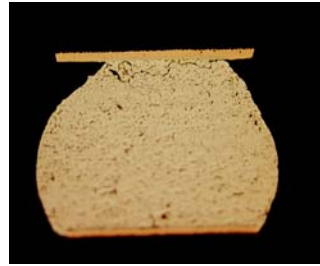
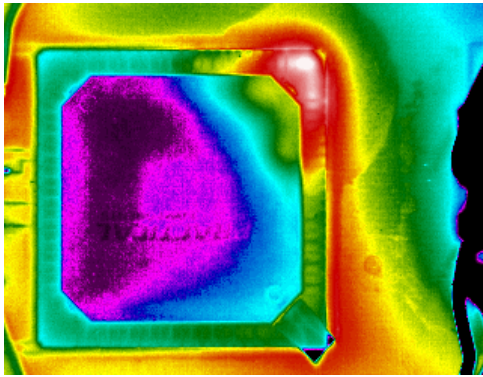
### **Conclusion:**

The failed balls that were found in channels on BGA 352 had higher resistance. As resistance increases the solder balls become hotter and this heat was detected with an infrared camera. Location of failed solder balls was confirmed by metallography and comparison back to thermal image pictures. These results indicate that thermal imaging of the board using an infrared cameras is a good method of locating failed solder balls on ball grid array chips.

### **Acknowledgements:**

The author would like to thank the Maine Space Grant Consortium for their funding and the Marshall Space Flight Center for providing facilities support. The author would also like to thank Jeff Brown for giving me the opportunity to work in the department and Mark Strickland for being my mentor in the 10 weeks at MSFC. Additional thanks goes out to Terry Rolin, Garry McGuire, David Geist, and Jim Blanche for providing a helping hand through my research. Without the people listed above, this work would have never been possible.

**Pictures of Some Thermal Images and the Corresponding Solder Balls**



Jason McGann  
University of Maine

Participating at the Glenn Research Center

Project Title “Using Visual Basic 6 To Automate Solar Cell IV  
Curves”

NASA Mentors Dr. Sheila Bailey and David Scheiman

## **Abstract**

This paper provides an overview of the steps and equipment used to automate the measurement of solar cell IV (current vs. voltage) curves using Microsoft Visual Basic 6 across the General Purpose Interface Bus (GPIB IEEE - 488) bus.

## **Introduction**

Glenn Research Center's solar cell evaluation laboratory (solar cell efficiency and spectral response measurement) is faced with updating the hardware and software used to operate their test equipment. Currently they are using Intel i386 (late 1980's) era equipment running HP (Hewlett Packard) Basic to control equipment operation, data acquisition, and data output of solar cell characteristics. At the moment the system works fine but if the i386 computer were to fail it would be very difficult to find a suitable replacement. Unfortunately the original software will not run on today's computers as the operating systems found on today's PCs are vastly different from those found on PCs 15 years ago. Due to the relative simplicity of the programs combined with the potential for additional features found in newer programming languages it was decided that rewriting the software in Visual Basic was the best course of action.

## **Problem**

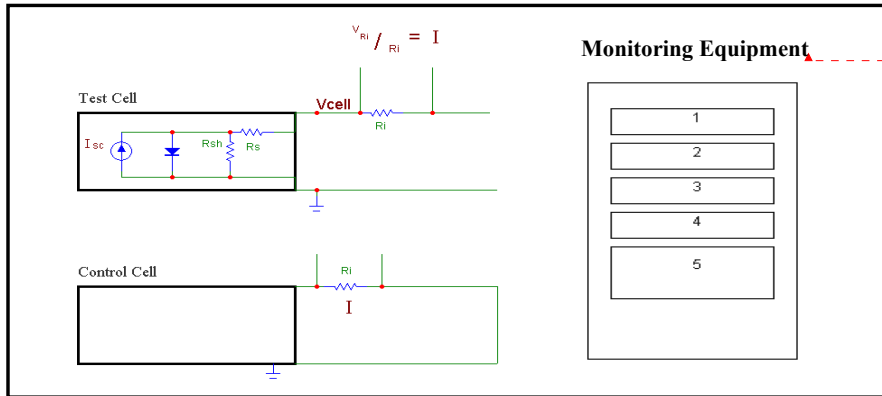
The problem was to write Visual Basic 6 code that would interface with Fluke 8520 and Fluke 8505 digital multimeters, a Fluke 2205A multichannel switch, and an HP 6129C variable DC powersupply across the IEEE-488 or **General Purpose Interface Bus (GPIB)**. The program was to take company name, cell material, as well as other plain text information, in addition to numerical parameters such as the test cell's area and a control cell's current as inputs. The program then has to generate the current-voltage characteristics, or the IV curve, of the solar cell under test, as well as to measure temperature from a thermocouple, thermistor, or **Resistive Temperature Detector (RTD)** and display these values in real-time. The test cell current and voltage, control cell current, and test cell temperature all had to be triggered and read simultaneously for each point the IV curve. The program was then required to process the data and scale the test cell's current according the instantaneous light intensity and output values such as the open circuit voltage ( $V_{oc}$ ), short circuit current ( $I_{sc}$ ), fill factor (FF), overall cell efficiency, etc. Input and output data had to be recorded into a text file, and be printed in the form of a summary chart or a 2-D graph. All this to be done in a traditional windows environment (pull-down menu, mouse clicks, and buttons) structured in a way for ease of use and operation. Also, the code was to be written to provide good program flow for easy modification and subroutines that can be adapted to other programs.

## **Method of Solution**

The description of the solution will be addressed in 3 parts. The first section provides a general overview of the hardware setup necessary for this solution. The second section

covers software methods for creating and displaying an IV curve and deriving important cell characteristics. The third section is brief and will cover data output and more specifically the visual basic control VSView.

### Overview of Test Equipment



1. Fluke GPIB addressable switch allows for :
  - a. Routing of **Digital MultiMeters (DMM)** to all different kinds of test equipment.
  - b. Control of UV blocking window for operator protection.
  - c. Source of trigger mechanism for simultaneous readings.
2. Fluke 8520 DMM is used in this application to measure the voltage across the test cell.
3. Fluke 8505 DMM is used in this application to measure the current output of the test cell (voltage / resistance).
4. Fluke 8520 DMM used as an ohmmeter and voltmeter depending on the selected temperature sensor.
5. HP 6129C Bi-Polar Variable DC Powersupply is used in this application to provide the range of bias points.

### Hardware Interface

A Measurement Computing (PCI-GPIB-300K) PCI (standard 32-bit internal interface) to GPIB card was installed in a Microsoft Windows 2000 / AMD Athlon XP computer system. Contained in the installation package for the PCI card are the files gpib-32.dll, cbic32.exe, cbconf32.exe, gpib-32.bas as well as a sample Visual Basic program. The digital multimeter's electronic address (0 – 31) is set with dip switches on the back of the device. The file cbconf32.exe is used to specify a name and address for each of the devices connected to the bus. Each multimeter was simply given the name "DeviceXX" where XX is the electronic address. Visual Studio 6 was used as the development package for this software. After adding the gpib-32.bas file to the project the devices were readied for use with the following code:

```

General Declarations
Dim CellCurrent%, CellVoltage%, MonitorCell%,
PowerSupply%, Controller%, TempMeter%,
TempOhm%

```

```

Private Sub Form_Load()
Call ibfind("Device23", CellCurrent)
Call ibfind("Device20", MonitorCell)
Call ibfind("Device22", CellVoltage)
Call ibfind("Device09", PowerSupply)
Call ibfind("Device16", Controller)
Call ibfind("Device24", TempMeter)
Call ibfind("Device25", TempOhm)
End Sub

```

The ibfind command stores the electronic addresses of the devices into the variables CellVoltage, CellCurrent etc. The devices can now be written to and read from using the subroutines found below.

```

Public Sub WriteCommand(TheDevice%, Cmd$)
CheckBus 'checks GPIBInProgress status loops until false
GPIBInProgress = True
ibsta% = ilwrt(TheDevice%, Cmd$, Len(Cmd$))
If TheDevice <> Controller Then
If (ibsta% And EERR) Then
TheDevice% = -1
Else: End If
ibsta% = ilwait(TheDevice, CMPL + EERR)
If (ibsta% And EERR) Then
TheDevice% = -1
Else: End If
Else: End If
GPIBInProgress = False
End Sub

```

```

Public Sub ReadValue(TheDevice%, rdbuf$)
Dim NULLCHAR As Integer
CheckBus
GPIBInProgress = True
BUFSIZE& = 256
NULLCHAR = 2
rdbuf$ = String$(BUFSIZE, NULLCHAR)
ibsta% = ilrd%(TheDevice, rdbuf$, BUFSIZE&)
If (ibsta% And EERR) Then
rdbuf$ = "---"
TheDevice% = -1
'ReadValue% = -1
Else
i = 1
Do While Mid$(rdbuf$, i, 1) <> Chr$(NULLCHAR)
i = i + 1
Loop
rdbuf$ = Left$(rdbuf$, i - 2)
'ReadValue% = 1
End If
GPIBInProgress = False
End Sub

```

While the demonstration program found in the installation package provides the framework for error reporting, partly due to inexperience, these error codes did not seem to be helpful. Instead the read function was written to return “---“on error. This allowed for the IsNumeric() function to yield false and the val() function to yield zero if there was ever a problem with a read.

Once the hardware was correctly configured and the code above was in place it was a relatively simple matter to issue commands to the devices and to read the returned values. While the syntax of the commands will vary from device to device the code below shows the basic framework.

```
Dim strValue as String
Dim dblNum as Double
    Writecommand( Controller, "01,")
        Wait( 0.1 )
    WriteCommand (Powersupply, "2.000100") 'set power supply voltage to
    WriteCommand (CellVoltage, "!") 'tell meter to read cell voltage
        Wait( 0.1 )
    ReadValue ( CellVoltage, strValue)
    dblNum = val(strValue)
```

Switch bounce is another hardware issue that was considered. At least a 0.1 second delay was implemented whenever relays were switched. Delays should be implemented using the system clock, as using counting loops for delays yield different delay durations depending on the speed of the computer system. Additional delays were added between writes and reads to the Fluke 8520 and 8505. A delay of 0.1 seconds seemed to be enough to allow the transients in these particular meters to decay.

Creating the IV curves and processing the data after these issues have been addressed becomes an exercise in Visual Basic and in GPIB device syntax more than interfacing the PC to the real world.

## Software

The code required to have all the devices sample simultaneously is relatively easy to implement on the Fluke 85XX devices. A command is issued that sets the meters to wait for a trigger signal from the controller. When the GPIB switch activates the meters take a reading.

A Visual Basic control was created that would accept input in the form of a text file formatted as X,Y and display the resulting graph based on the range of the input data. The control looked at the range of the X and Y data independently and chose a 1, 2, or 5 \* 10<sup>3i</sup> (where i is a whole number) as a scale for each axis. Additionally the control would center the data at the center of a 10 by 10 grid. The control graphed only 1 line and connected points according to the order in which they were read from the file. A control was developed with the idea that it could be reused in future programs .

In addition to the IV curve itself there are seven values of interest: the open circuit voltage ( $V_{oc}$ ), the short circuit current ( $I_{sc}$ ), the maximum power output from the cell ( $P_{max}$ ), the current and voltage at the maximum power point ( $I_{max}$  and  $V_{max}$ ), the fill factor (FF) and the overall efficiency of the solar cell under test.

Testing is started at  $V_{oc}$  (zero current through the cell) as it is found precisely by open circuiting the test cell and finding the voltage difference at its terminals. Independent of the sign of  $V_{oc}$ , the voltage placed on the powersupply must go from this value towards zero.

The user selects a number of points in the curve and step size becomes  $V_{oc}$  divided the number of points. The value of the DC powersupply is then decremented in magnitude by this step size and each time the voltage, current, and the temperature of the test cell is logged. The user selected number of points is only an estimate however because the voltage across the test cell and powersupply voltage do not track exactly due to the series resistor. Therefore the powersupply must be decremented past zero until it is opposite the sign of  $V_{oc}$ . The test is completed when the sign of the *voltage on the test cell* is opposite the sign of the open circuit voltage.

At run time the raw data was plotted. After completion of the curve however the current values obtained are scaled depending on the current output of the control/monitor cell. The changes in current output of the control/monitor cell show small variations in intensity of the light source over short amounts of time as well as drifting of the light source's intensity over longer durations.

The short circuit current (zero voltage across the cell) is an interpolation between the last point, the first time point where the cell is reverse biased, and the second to last point. Interpolation of this point is important as inefficient cells can have IV curves with a significant slope as they cross the Y-axis. In this case, neither the last nor the second to the last point is representative of the short circuit current.

The maximum power point is found by simply sifting through the data set looking for the largest current and voltage product. Additional accuracy is gained by using a linear fit between the  $P_{max}$  and the point adjacent to the left and second linear fit between the  $P_{max}$  and the point adjacent to the right. One hundred interpolated points were then tested on each of these two lines in search of a new  $P_{max}$ . This interpolation procedure was not used if for some reason the  $P_{max}$  was either the first or the last value in the data set.  $V_{max}$  and  $I_{max}$  were then the X and Y components of the  $P_{max}$  point.

The fill factor was calculated as the interpolated  $P_{max}$  value over the product of  $V_{oc}$  and  $I_{sc}$  and is a measure of the squareness of the curve. The cell efficiency was the interpolated  $P_{max}$  point over the product of the area and AM0 power density.

## Data Output

Data output was accomplished by the use of a third party software tool called VSView, it is similar to Postscript. This visual basic control allowed for consistent graphs independent of the printer model or resolution and allowed for higher resolution printing than what was inherent in Visual Studio 6. An XY graph for each test as well as a summary chart of all the tests run during a session was implemented. VSView allows for precise placement of text and lines on the printed page defined in inches. In addition it has a print preview function that allows for zooming and scrolling functions, saving hours of programming time.

## Conclusions

Test software will likely be run over and over again and should be as simple and bug-free as possible. In the end it was decided that when writing this type of workhorse software that features should be secondary to writing solid simple code. The most significant conclusions reached throughout the course of this project were:

- a. Master the system and test procedure before writing even single line of code. In programming it seems like jumping headfirst into the problem leads to the rewriting of code.
- b. Clearly define all or as much of the inputs and outputs to your program as well as any required features before you write any code. Adding features in the middle takes longer and makes for poorly written code and should be avoided when possible.
- c. Stay away from the object-oriented style as much as possible. It is more efficient to write a few small programs to tackle multiple tasks instead of trying to lump them all into one. The more you limit the user's control options the faster it is to troubleshoot bugs. In addition a series of less complex programs lessens the chance that there are strange interactions between parts of the program.
- d. Define a single uninterruptible subroutine that captures input from the form and stores for later use. This data should remain unmodified throughout the program. In addition write a single uninterruptible subroutine that takes all the raw data and processes into output data. After processing the output data should remain unchanged through the remainder of the program. The more you nail down where and when program data is modified the quicker the troubleshooting and more solid the code.
- e. A global function that takes a double number and a number of significant digits and returns the number with the correct number of digits and metric suffix is invaluable. A global function that can condition any number for display with the correct decimal places and a metric suffix will save a lot of time in the long run.

- f. The debugging toolbar in Visual Studio 6 is an incredibly powerful tool for quickly finding problems with the code. One function allows you to execute a line of code with every button press including any code executed in subroutines or functions. The second allows you to skip code in a subroutine or a function and view only its result.
- g. Converting code to Visual Basic is definitely a viable solution to the problem of aging hardware and software. Visual Basic is quite easy to learn, provides a familiar Microsoft Windows-like interface and has the required DLL's to talk with equipment over the GPIB bus.

### **Acknowledgements**

This paper is to be a brief explanation of the process used in the lab to convert antiquated software to Visual Basic. Much of work was done by Dave Scheiman, the original author of the HP basic code, and in the case of the writecommand and readvalue subroutines an unknown author (presumably the company Measurement Computing). I was brought into write the code but the test methodology was created long before I arrived. I do not intend to take any credit for anything except the actual program itself which at best joined many other people's work together. Thanks again to Dave Scheiman for his help and support through the duration of my summer internship. In addition thanks to the Maine Space Grant Consortium and the USRP Program at Glenn Research Center.

Sarah J. Sandwick  
University of Southern Maine

Participating at the Johnson Space Center

Project Title “Combined Effects of Space Radiation using the Tool  
of Earth-bound Heavy Metal Radiation ( $^{56}\text{Fe}$ ) and Microgravity on  
Mammalian Cells”

NASA Mentor Dr. Steve R. Gonda

## Abstract

Cells genetically engineered to contain >60 transgene inserts per cell of the cII gene, a small 294 bp gene, have been accepted for use in mutagenesis assays. Previous work employed these cells in the form of *in vivo* models using Big Blue rodents and *in vitro* models using the two-dimensional (2D) monolayer. The 2D method has the disadvantage that cells grow in a single layer on an artificial surface. When compared to the 2D model, the *in vivo* model is seen as a more realistic tissue model, but harder to manipulate. The 3D model has shown more DNA damage than the 2D monolayer model. The effects of damage in the 3D model are more microcellular tissue-like nature than the 2D, but comparable damage to the *in vivo*. A hybrid, a three-dimensional (3D) model using Cytodex 3™ beads, has been developed incorporating the main advantage of the 2D culture, which is cell culture without the concern of animal care, and the main advantage of *in vivo*, which is accuracy. In this study, a comparison of techniques between an accepted protocol at University of Texas Health Science Center at San Antonio (UTHSCSA) and newly created 3D model protocol at Lyndon B. Johnson Space Center (JSC) were done to determine if the procedures at JSC could be accepted. Liver obtained from wild-type and DNA polymerase β heterozygous knockout (DNA polβ) Big Blue rats were frozen and sent to JSC. DNA was extracted and the rates of mutational frequency were determined by the cII assay according to manufacturer's instructions; dividing the mutant plaques formed at 24C by the total plaques formed at 37C. The comparative results of mutation frequencies are as follows: wild type  $5.75 \times 10^{-5} \pm 0.88$  (UTHSCSA) and  $4.77 \times 10^{-5} \pm 0.62$  (JSC) and DNA polβ  $4.15 \times 10^{-5} \pm 0.58$  (UTHSCSA) and  $2.44 \times 10^{-5}$  (JSC). (Note the JSC DNA polβ sample was only performed once.) Both of these results are normalized to the control mutation frequency. The 3D model protocol at JSC has similar results to UTHSCSA protocol, allowing the JSC protocol to become an accepted procedure to measure mutation frequency.

## Introduction

### RADIATION:

Radiation is ranked as the highest risk to astronauts traveling outside of low earth orbit (LOE) by NASA and the National Research Council. Astronauts are exposed to high amounts of high-atomic-number energetic ionizing particles, much more than humans that only survive and thrive within Earth's atmosphere. This is due to the Earth's atmosphere ability to block most of this radiation, which in turn enables life upon this planet. Astronauts who fly out of the protection of our atmosphere are at risk due to the exposure to higher levels of radiation. The effects of radiation exposure include increased incidence of cancer, lowered immunity, and damage to cells and their chromosomes.

#### MICROGRAVITY:

The effects of microgravity have been observed on many of tissue systems of astronauts, including the immune system. Loss of immune surveillance and activation, and the potential degradation in repair mechanisms of cellular and genetic damage (mutations, double strand breaks) are important risks that must be resolved.

#### WHY MOVE TO A NEW SYSTEM:

The Big Blue rat liver tissue received from University of Texas Health Science Center at San Antonio is an *in vivo* model of the Big Blue cells, whereas the 3D aggregates are the cell-line model. What are Big Blue cells? In a Big Blue cell-line or animal, every cell contains roughly 60 copies of an inserted gene sequence in their DNA. In this assay, the cII gene is the selected gene inserted. Primarily, studies performed previously have been on 2D systems. These 2D systems include a monolayer of cells grown upon a solid surface. This is not entirely representative of the normal interactions between cells *in vivo* due to the interaction between the cells and the non-cell surface on which they are adhered. The problem with *in vivo* is that with difficult removal of a particular organ, loss of important cells may occur. *In vivo* also has problems with getting all exactly the same sizes of experimental animals, and even if the animals may be similar in size, their organs may be different. 3D aggregates cut down on the problems associated with *in vivo* work, but fulfills the same role.

#### cII GENE:

Studies have been done to examine the effects of radiation at the chromosomal, gene and molecular levels. Radiation does not seem to target particular genes, but affects genes randomly. If one would examine the frequency of mutation in a cell's DNA, it should be representative of all of the genes within the exposed cell. Big Blue cells contain multiple identical copies of inserted gene sequences in their DNA. This sequence contains the cII gene, which will be the gene that we will measure space radiation-induced mutations. The cII gene is sensitive, accurate, and flexible. It is sensitive it can detect small mutations in DNA sequence and also since there are many copies within a single cell, there can be more detection. The cII gene assay is more accurate than others because it is not a subjective color screening, so there will be fewer false positives. The cII gene can be used in different assays.

#### **Problem**

Overall Problem: The problem is heavy iron particles in the space atmosphere and microgravity environment affect the astronaut's ability to prevent cellular and molecular damage and consequently its repair is also hindered. Although nothing can be recreated perfectly, models are a good for studying effects. In this particular case, this study addresses the effect of a simulated microgravity environment on space radiation-induced mutations in two-dimensional (2D) monolayers and three-dimensional (3D) aggregates. This project has the goal of determining the effect of a simulated microgravity environment on space radiation-induced mutations in two-dimensional (2D) monolayers and three-dimensional (3D) aggregates.

Objectives:

1. To determine if simultaneous exposure to microgravity conditions changes DNA mutation frequency and types.
2. Determine whether the combine effects of radiation and microgravity are similar to the effects of radiation in unit gravity.

Specifically my projects: To perfect the current NASA space radiation mutagenesis protocol into an accepted protocol for the mutagenesis assay for the recent 3D aggregate model.

Project:

To validate the mutation analysis protocol for the 3D Big Blue in vitro model using the University of Texas Health Science Center at San Antonio's Big Blue in vivo liver tissue, the goal is to test our DNA extraction and mutagenic assay efficiency of the 3D aggregates and to establish the 3D aggregates as a working model that most accurately represents astronauts in mission. In order to perfect the protocol, I will test two different types of agar by examining plating efficiency which would allow me to confirm both agar formulations meet the requirement for the Big Blue assay. The Big Blue agar with the addition of X-gal is specifically used for the lac operon, but the Big Blue agar seemed to have a similar formula to the TB1 agar. With the switching over to the cII gene, the Gonda laboratory is checking to see if this agar can still be used. The difference between the agars is yeast and MgSO<sub>4</sub> is in the Big Blue agar formulation created by Stratagene. The composition of both of them that is similar is sodium chloride, casein peptone and thiamine hydrochloride.

Objectives:

1. To compare the mutation frequency we obtained in our lab with our Big Blue protocols with the mutation frequency determined by University of Texas Health Sciences Center at San Antonio on the same live tissue.
2. In the long-term range, this correlation of exposure could help research on prevention of exposure, treatment of the effects, or countermeasures if prevention cannot be achieved.
3. To validate two Big Blue agar formulations in support of genotoxic evaluations of space radiation in mammalian cells using the Big Blue model.

**Methods:**

Previous work

NASA has developed and optimized a three-dimensional (3D) tissue-like model using fibroblasts and epithelial cell lines that are genetically engineered to contain a high density of the lac Z gene (>65 targets/ cell) for genotoxic assessment of radiation (<sup>56</sup>Fe) and simulated microgravity (created through a NASA developed bioreactor) at the gene and molecular level. The importance of 3D cultures is that the 2D monolayers have seen different results in previous experiments than the 3D cultures due to its cellular

environments. More specifically, the 3D models have greater mutation rates, various types of mutations, and large deletions have been seen at high levels of  $^{56}\text{Fe}$ .

FIGURE 1: NASA designed bioreactor



**MUTAGENIC ASSAY:**

In the Big Blue Mutagenesis assay, the cII gene has a piece inserted into big blue cells. This insert contains the c 1857 gene, which activates the cI repressor at 37 C, allowing titration of all inserted cII genes, but at 24 C only the mutant cII can grow. The purpose of this cII gene is that it is a known region in the genome and can be investigated for mutation due to the insult from the  $^{56}\text{Fe}$  and the simulated microgravity.

A transgenic target, cII gene, was placed in a vector and inserted into a cell in at a high copy number. These cells were grown on micro-carrier beads then the cell-bead matrix, observed as a tissue equivalent, was placed into a simulated microgravity environment and irradiated with  $^{56}\text{Fe}$  (simulated space radiation). This was done at Brookhaven National Laboratory.

This is where my project would start for the checking of the current mutagenesis assay before we used the protocol on the Brookhaven samples. My project was to purify the DNA from the San Antonio provided samples from Big Blue rodents, B1, B2, T2 to show that our mutagenesis assay provides similar results to the University of Texas Health Science Center at San Antonio who did the same thing with their protocol. Our purification was done using Chloroform and ethanol. Once the transgene was purified, it was packaged into the phage. The phage then transformed the bacteria, G1250, this gave the packaging efficiency. The transformed bacteria were then plated at two temperatures. At 37C as titration plates, giving the total cII inserted genes and at 24C as mutant plates which gives the total mutated cII genes inserted. When plating control phages for this experiment, I tested the two different agar formulations.

**Data**

TABLE 1: Obtaining the University of Texas Health Science Center at San Antonio’s Big Blue Liver tissue’s mutation frequency

Sample	Tissue Weight <i>mg</i>	OD $\frac{260}{280}$	[DNA] $\frac{\mu\text{g}}{\mu\text{L}}$	Volume <i>ug</i>	Total DNA isolated <i>ug</i>	[DNA isolated] $\frac{\mu\text{g DNA}}{\text{mg tissue}}$	[DNA isolated] $\frac{\mu\text{g DNA}}{\text{g tissue}}$	Mutation Frequency <i>Big Blue cII assay</i>	Mutation Frequency Normalized to Control
B1	540	1.82	4.01	75	301	0.56	557	$5.77 \times 10^{-5}$	$4.15 \times 10^{-5}$
B2	512	1.90	6.80	300	2045	3.99	3993	$6.96 \times 10^{-5}$	$5.4 \times 10^{-5}$
T1	645	1.89	8.65	75	649	1.01	1006	Needs to be repeated	N/A
T2	424	1.80	3.60	300	1080	2.55	2547	$4.00 \times 10^{-5}$	$2.44 \times 10^{-5}$

**TABLE 2:** Sample Mutant Frequency Comparison  
**Table 3:** TB1 and BB plating efficiency of JSC results and UTHSCSA results

	<i>TB1</i>	<i>BB</i>
<b>Plating efficiency</b>	$1.56 \times 10^{-5}$	$1.90 \times 10^{-5}$
<b>Standard Deviation</b>	$1.64 \times 10^{-6}$	$5.16 \times 10^{-6}$

	<b>B (wild type)</b>	<b>T (DNA pol β)</b>
<b>JSC</b>	$4.77 \times 10^{-5} \pm 0.62$	$2.44 \times 10^{-5}$
<b>UTHSCSA</b>	$5.75 \times 10^{-5} \pm 0.88$	$4.15 \times 10^{-5} \pm 0.58$

FIGURE 1: The frequency of mutation in samples B1, B2, and T2 found through purification and NASA mutagenesis assay protocol.

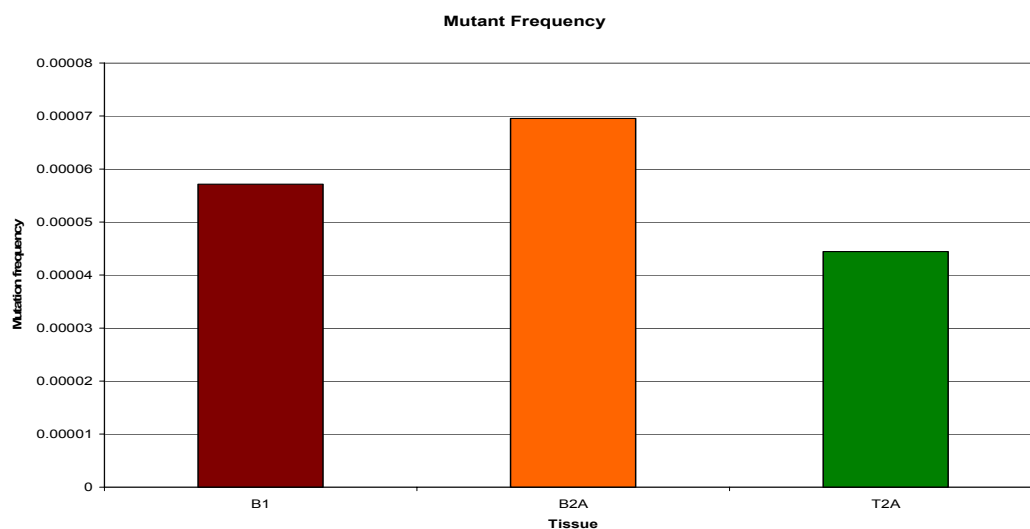
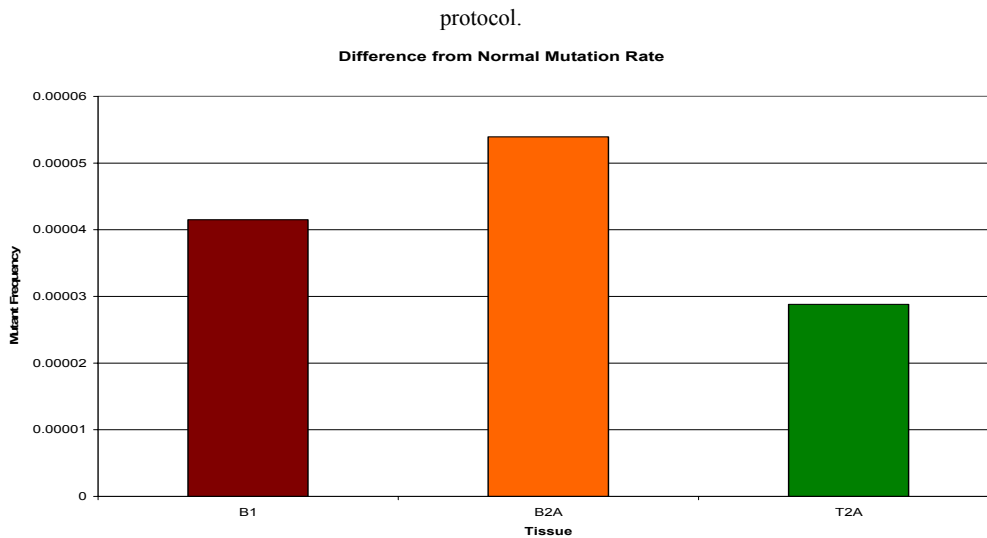


FIGURE 2: The frequency of mutation with the background subtracted out in effect “normalizing the data” in samples B1, B2, and T2 found through purification and NASA mutagenesis assay



## Conclusion

The space radiation mutagenesis assay done on the wild type liver cells had similar results.

The DNA was extracted and the rates of mutational frequency were determined by the cII assay according to manufacturer's instructions; dividing the mutant plaques formed at 24C by the total plaques formed at 37C. The comparative mutant frequencies, normalized according to controls, are as follows: wild type  $5.75 \times 10^{-5} \pm 0.88$  (UTHSCSA) and  $4.77 \times 10^{-5} \pm 0.62$  (JSC) and DNA pol $\beta$   $4.15 \times 10^{-5} \pm 0.58$  (UTHSCSA) and  $2.44 \times 10^{-5}$  (JSC). (Note the JSC DNA pol $\beta$  sample was only performed once.) Although the DNA pol $\beta$  needs to be repeated, I would say that the NASA mutagenesis assay should be considered an accepted protocol. The next step is to do the space radiation assay on the samples that were exposed to radiation and simulated microgravity to see the results of these coupled environments on mutation rates. In this assay either agar could be implemented because the tested agars resulted in similar results. The TB1 agar had a plating efficiency of  $1.56 \times 10^{-5} \pm 1.64 \times 10^{-6}$  while BB agar had a plating efficiency of  $1.9 \times 10^{-5} \pm 5.16 \times 10^{-6}$ . The space mutagenesis assay will improve our knowledge in what mutations which occur due to space radiation and simulated gravity. Hopefully this information will assist in advancing the knowledge of mechanisms which cause them. This furthers our ability to preemptively stop the mutations from occurring.

## Acknowledgements

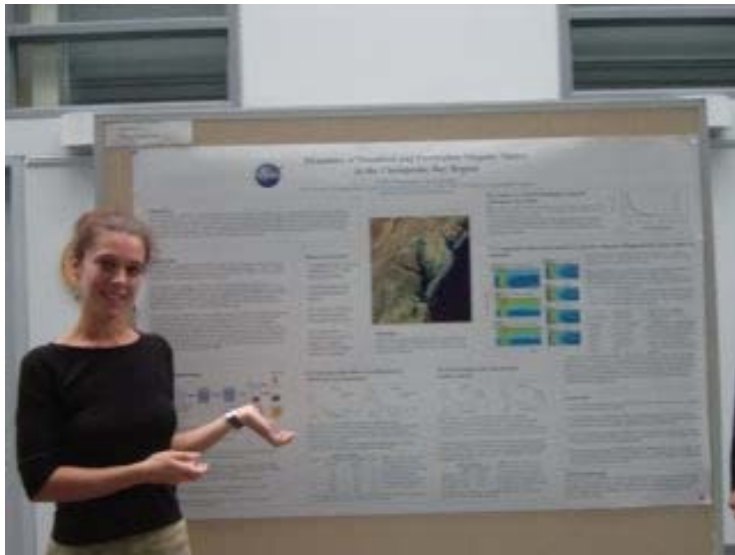
Author would like to thank Dr. Steve Gonda for his guidance and laboratory space. The author would also like to thank Kamal Emami and Dr. Rachael Casey for assistance and expertise in molecular biology techniques. This research was supplied through the Maine Space Consortium Grant.

Heather Throckmorton  
University of Southern Maine

Participating at the Goddard Space Flight Center

Project Title “Dynamics of Dissolved and Particulate Organic  
Matter in the Chesapeake Bay Region”

NASA Mentor Dr. Antonio Mannino



### *Acknowledgements*

Thanks to MSGC for the funding to make this research possible; Dr. Mary Russ who contributed a great deal to the project and to my experience; special thanks to Antonio Mannino for his oversight and guidance of my work at NASA GSFC during the summer of 2005. Standards were purchased from the National Institute of Standards and Technology (NIST) and the International Humic Substances Society (HISS).

Carbon is an essential element to all living organisms. Cycled between the atmosphere; the terrestrial biosphere; and the hydrosphere, carbon supplies nourishment to plants and animals and also works as a greenhouse gas to maintain climatic conditions that are sufficient to support life. Carbonates and bicarbonates are dissolved forms of carbon dioxide that serve as nourishment to phytoplankton, which are important components of the marine food chain. Carbon that has been isolated from the natural carbon cycle is stored in a number of long-term reservoirs, which could be considered either a “source” or “sink” with respect to the active carbon budget. One important example of this is the burning of fossil fuels. Oil, coal and natural gas are organic materials which have undergone metamorphosis for hundreds of thousands of years. The burning of these natural resources transfers carbon from long-term storage back into the atmosphere in the form of carbon dioxide. Although some carbon continues to be buried and transferred again into long-term storage, the overall effect is a net increase of carbon in the atmosphere. Atmospheric carbon dioxide levels are an expression of the delicate balance between photosynthesis and respiration, and any disturbance in this exchange will have inescapable effects on global climate and the natural ecosystem. Monitoring these changes is not only important to understanding the Earth system, but will enable us to better manage natural resources for the future.

Coastal ocean waters represent a vital link in the global carbon cycle. Terrestrial organic matter is delivered via riverine export to coastal waters, where the material becomes either consumed through biogeochemical processes or is distributed throughout the world's oceans. The dissolved organic carbon (DOC) pool is roughly equivalent to levels of atmospheric carbon dioxide; if excess DOC builds up in oceans, oxidation through microbial degradation or photooxidation will transfer this material into the atmosphere as CO<sub>2</sub>. The fate of this material is an important clue to understanding the global carbon cycle and the Earth system.

There are a number of techniques with which to study the dynamics of organic materials in seawater. Both dissolved organic matter (DOM) and particulate organic matter (POM) exhibit optical properties that are detectable through spectral analysis. For practical purposes, satellite imagery is the most useful method for assessing large scale geographic regions. But because chromophoric dissolved organic material (CDOM) and POM are not the only components that contribute to the color of seawater, adequate classification of ocean water from satellites requires validation based on seawater sampling and laboratory analysis. Eventually, a mathematical relationship can be established between the composition and the optical properties of seawater for a particular region. This would

enable accurate interpretation of the composition and concentration of the chromophoric constituents of oceans based only on satellite imagery.

The research conducted by Antonio Mannino, Mary Russ and Heather Throckmorton aims to investigate the sources, sinks and standing stocks of DOC, POM, and CDOM in the Chesapeake Bay region and in adjacent Atlantic Ocean waters. This research will



provide insight into the seasonal variability of terrestrial organic matter, black carbon, DOC and CDOM in this area. We are interested in quantifying and understanding algal production of DOC, and in researching the optical and chemical effects of photodegradation on DOC. The long-term objective is to develop algorithms with which to monitor CDOM and DOC using the MODIS satellite remote sensing instrument.

Preliminary research conducted by Heather Throckmorton during the summer of 2006 includes (I) evaluation of the effect of acidification on CDOM spectral absorbance; (II) DOM isolation and concentration method analysis; (III) analysis of CDOM distribution along the Chesapeake Bay plume; and (IV) comparative fluorescence analysis of seawater along the Chesapeake Bay plume relative to standards. Each research topic will be considered in the following discussion.

**Fig 1 Field site** Large volume seawater samples were collected aboard the R/V Fay Slover at the mouth of the Chesapeake Bay in May 2005.

Seawater samples are collected aboard a research vessel at variety of depths throughout the Chesapeake Bay, the Delaware Bay, and adjacent Atlantic waters. Water is pumped through 0.2 $\mu$ m filters to remove particulate matter. The water is acidified to a pH of 2.5 in order to prevent microbial proliferation and DOM degradation, and to protonate charged functional groups. This is a prerequisite for the DOM isolation and concentration procedure, which utilizes SPE cartridges containing C-18 bonded silica packing material. The isolated DOM is desalted with ultrapure water and is eluted with methanol through the SPE cartridge. Spectral absorbance is measured with a UV-Vis spectrophotometer using 100mm pathlength cylindrical cells, and referenced to ultrapure water. Fluorescence is measured using an HPLC instrument equipped with an autosampler photodiode array and fluorescence detectors.

I) The acidification procedure is important not only for the preservation of organic material, but also in preparation for SPE extraction of DOM. Because the spectral absorbance of CDOM is applied as a standard measurement for DOM levels, it is crucial that this method not impact the optical properties of the seawater samples. In order to evaluate this method, I compared several spectral absorbance measurements of natural seawater with seawater that had been acidified. The calculated slope values for these spectra displayed less than a 10% standard deviation. Results indicate that there is no

significant variation between natural seawater and seawater that is acidified.

II) The C-18 bonded silica cartridges have been previously shown to effectively isolate DOM. In order to evaluate how much DOM is extracted, I compared absorption coefficient spectra for seawater before and after having undergone SPE filtration, as well as the spectrum for the isolated CDOM (SPE extract), normalized to the original seawater volume. Two representative spectra are displayed below.

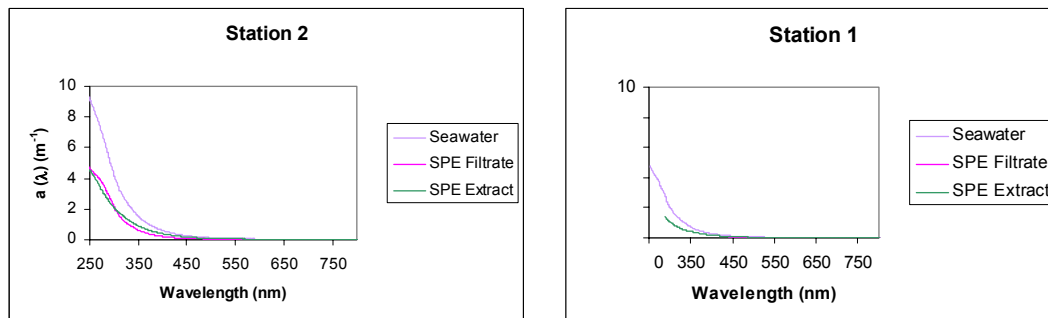


**Fig. 2** Figures A and B display absorption coefficient spectra for seawater before and after having undergone SPE filtration, as well as the spectrum for the isolated CDOM (SPE extract). Note that the seawater represented in figure A is of estuarine origin, whereas the seawater represented in figure B was collected from coastal Atlantic waters (see map, stations 1 and 2).

The graphs denote that a significant amount of DOM is isolated by the SPE cartridge. Additionally, the SPE filtration process isolated a greater percentage of DOM in figure A than in figure B, relative to the original seawater sample. This suggests that station 2 contains more terrestrial material, which is more susceptible to SPE extraction. Calculated slopes for absorbance coefficient spectra of water before and after having undergone SPE filtration display a relatively high variation, suggesting that certain DOM preferentially adsorb to the SPE cartridges.

III) The Chesapeake Bay is North America’s largest and most productive estuary. It acts as a drainage basin for over 64,000 square miles of land throughout New York, Pennsylvania, Maryland, Delaware, Virginia and West Virginia. In an effort to understand the dynamics of the organic material at the mouth of the Bay, absorbance coefficient spectra were collected from surface depths at stations 1, 2, 3, 4 and 7, following the Chesapeake Bay plume.

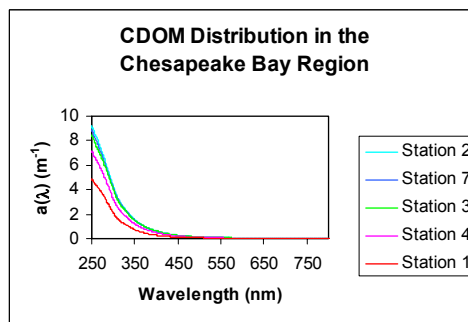
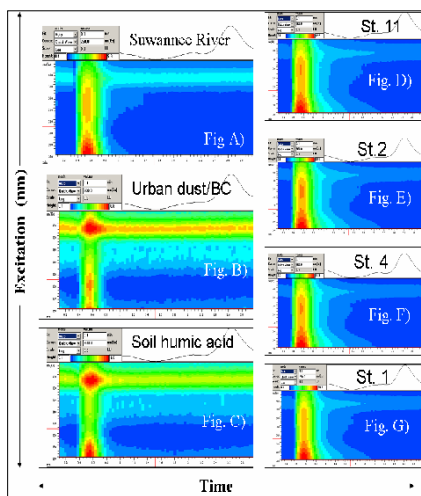


**Fig. 3)** Figure 3 displays absorption coefficient spectra for samples collected at surface depths (1m) from stations 1, 2, 3, 4, and 7 (see map).

The absorption coefficient spectra in figure 3 denote that the CDOM concentration is decreasing along the Chesapeake Bay plume, in a southeasterly direction. Station 1

contains the least amount of CDOM because it is located relatively offshore, and is not fed as strongly by the plume.

IV) Excitation scans were taken for seawater samples collected at stations 11, 2, 4 and 1 (see map), and for several previously obtained standards. The standards are composed of



important constituents of CDOM in coastal waters: black carbon; lignin phenols; and other terrestrial organic matter. These spectra allow for a qualitative comparison of the CDOM in seawater relative to the materials in these standards. Figure 4 displays excitation as a function of time.

**Fig. 4** Figure 4 displays excitation spectra for standards (A-C) relative to stations 11, 2, 4 and 1 (D-G), measured at an emission of 435 nm and with an excitation spectrum ranging from 230-410 nm.

**Fig. A** The Suwannee River standard (A) is composed largely of terrigenous material derived from wetlands of southern Georgia and Florida.

**Fig. B** The urban dust standard is composed of black carbon which is sourced mainly from fuel emissions. This standard is from Washington DC and processed to remove non-soot materials.

**Fig. C** The soil humic acid standard is composed of humic acids that have been leached from soils. Humic acids are produced as the result of abiotic reactions and microbial degradation of plant and animal debris. They are composed of a number of different compounds in varying amounts.

**Table 1** Table 1 highlights excitation peaks associated with figures 4A-4G.

	ex. max (nm)
Suwannee River	338-358, 250
Urban dust	387-397, 290-307
Soil HA	387-391, 250
Station 11	354-360, 250
Station 2	344-356, 250
Station 4	346-352, 250
Station 1	250

All spectra display excitation maxima in the UV range, with all but the urban dust/BC standard displaying excitation maxima at 250nm. The Suwannee River has an excitation peak ranging from 338-358 nm, which corresponds to excitation peaks at stations 11, 2 and 4. This is most likely due to the large amount of terrestrial runoff received by these stations. The seawater collected at station 1 does not display as strong of an excitation signal at this wavelength, most likely due to lower levels of terrestrial material; station 1 is located relatively offshore and not fed as strongly by the Chesapeake Bay plume. The soil humic acid standard displays an excitation peak at a slightly higher wavelength than the Suwannee River standard and corresponding stations. The excitation peaks for the urban dust standard do not correspond directly to excitation maxima for any of the stations, which does not necessarily indicate the absence of black carbon.

To summarize the previous discussion, a relative comparison of the absorbance coefficient spectra for natural seawater and seawater that had been acidified and neutralized prior to analysis shows that the acidification process has no significant effect

on the spectral absorbance of seawater. Thus, this method may be utilized in order to prevent microbial proliferation and DOM degradation, and for the purpose of protonating functional groups prior to isolating DOM through SPE extraction.

The C-18 SPE filtration process effectively isolates a sufficient amount of DOM from seawater, preferentially DOM of terrestrial origin. This is useful for isolating certain kinds of materials such as lignin phenols, which are compounds of particular interest for DOM analysis.

The absorption coefficient spectra collected for samples from surface waters of Chesapeake Bay convey that CDOM levels are decreasing along the Chesapeake Bay plume, in a southeasterly direction. Station 1 was found to contain the least amount of CDOM because it is located relatively offshore, and is not fed as strongly by the plume.

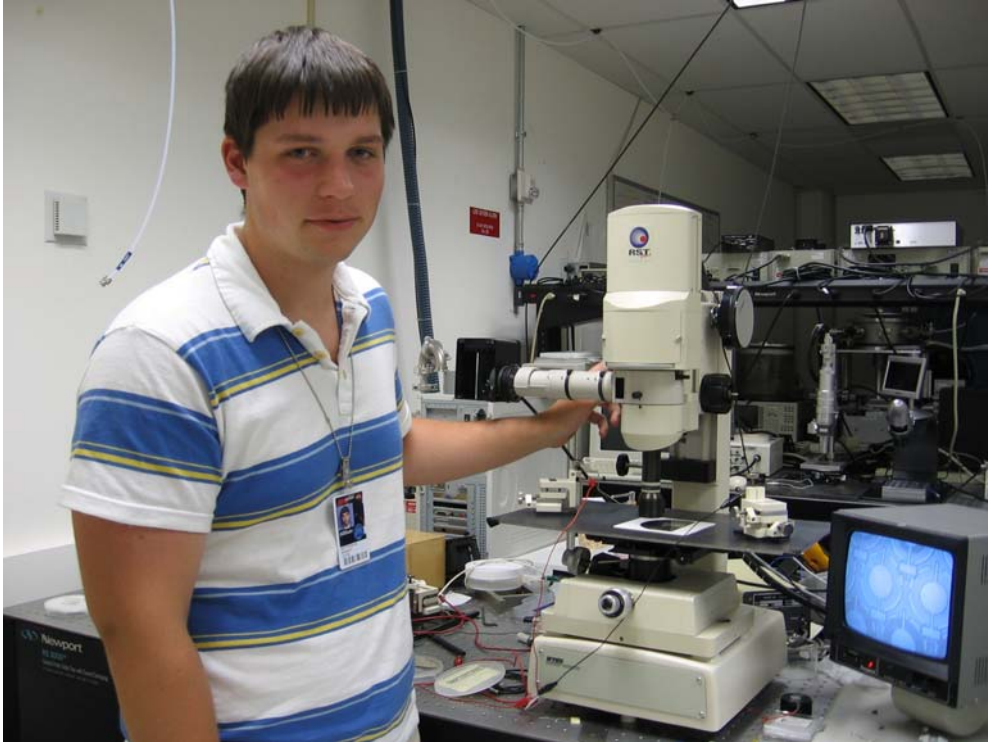
Stations located on the plume of Chesapeake Bay may contain terrestrial material similar to what is found in the standard obtained from the Suwannee River. Although no strong correlation was found between black carbon and the sampled stations, the presence or abundance of black carbon in this region is inconclusive from this study. Further investigation is necessary in order to make any strong conclusions.

Matthew W. Wright  
University of Maine

Participating at the Jet Propulsion Laboratory

Project Title “The Characterization of Thin Film Unimorph-  
Membrane PZT Microactuators”

NASA Mentor Dr. Eui-Hyeok Yang



Microactuators are versatile, low-cost, low mass electrical-mechanical devices that can be used in many applications. Microactuators consist of two electrodes sandwiching a PZT (a piezoelectric compound) film between them. The centers of the microactuators deflect when a voltage is applied across the electrodes. In order to correctly apply this technology for use, it is important to fully characterize the actuation behavior. Measuring the deflection profile as a function of the voltage of various microactuators is crucial. This measurement process has errors associated with it, so it is being studied to determine the accuracy of the data. In certain applications, microactuators may undergo many cycles of deflection; testing various microactuators through many cycles of deflection simulates these circumstances. However, due to an unknown issue, many of the microactuators exhibit defects that cause them to fail when voltage is applied to their electrodes. These defects do not allow for the acquisition of significant deflection profiles. Vibrations are the largest cause of error in deflection measurements, and the microactuators withstand continuous cycles of deflection, yet the cause of damage is still to be determined. Future projects will be needed to characterize the deflection profiles of various microactuators and to overcome the defects in the microactuators that are currently present.

Earth-based optical telescopes have recently grown larger and more complex, yet there is a practical limit that constrains the capable resolution of optical telescopes due to atmospheric conditions<sup>1-2</sup>. Wave-front error is a direct result of atmospheric turbulence, and it is the major limiting factor of optical observations in the visual spectrum<sup>1-2</sup>. Adaptive optics systems utilize modern technology to counter wave-front error<sup>3-4</sup>. The first adaptive optics system utilized piezoelectric actuators due to their accuracy, functionality and ability to endure periodic changes in displacement<sup>1</sup>. However, as adaptive optics designs grow larger and more complex, smaller and more accurate mechanisms are needed<sup>3-4</sup>. The thin-film PZT microactuators studied in this project are small, have a low mass, and have a nanometer resolution; thus, adaptive optics is one application of the thin-film microactuators studied in this project. As a result, our microactuators also need to withstand numerous cycles of displacements. Our thin film microactuators could also be used in optical switches and optical communications, both needing the same requirements for accuracy and endurance. In order for these microactuators to be used in adaptive optics systems and other applications, they must be first characterized so that the control of their motion is accurate and predictable.

For the remainder of this paper, the references to microactuators are reserved for the microactuators being studied in this project. The microactuators are piezoelectrically actuated; thus, a proper introduction to piezoelectrics need be presented. Piezoelectric crystals work off of the concept of the crystals being electrically poled. Electrical poling in any object is where one side of an object has more positive or negative charges than the opposite side of the object. Manufacturing piezoelectric crystals correctly results in the central molecule of the crystal, which has a positive charge, being displaced from the central position of the crystal (Figure 1)<sup>5</sup>. This displacement of the positively charged molecule means that the crystal is poled since there is now more positive charge on the side of the crystal with which the positive molecule displaced. If the poled crystal were to be in an electric field, then it would rotate to line up its poles with the field. For example, imagine a negative external charge near the poled crystal. This charge will attract the positive pole of the crystal and repel the negative pole of the crystal, causing the crystal to turn so that the positive pole of the crystal is closer to the negative charge and the negative pole is further from the negative charge. In a piezoelectric actuator, applying an electric field causes all of the piezoelectric crystals to align their poles with the electric field. This alignment of poles changes the dimensions of the actuator with immense accuracy, allowing one to accurately control a piezoelectric actuator.

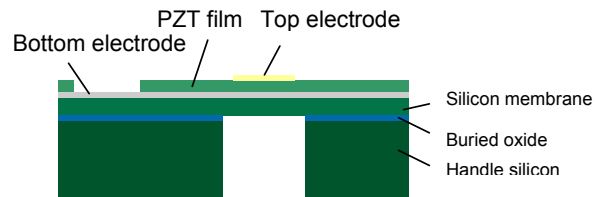
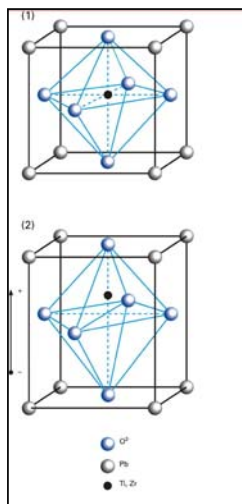


Figure 2: Sketch of thin film PZT microactuator system on a silicon wafer

Figure 1<sup>5</sup>: Diagram of Piezoelectric crystals un-poled in (1) and poled in (2)

The Microactuators studied in this project use Lead Zirconate Titanate (PZT), a piezoelectric compound, to actuate. The PZT layer is sandwiched between the top electrode (gold) and the bottom electrode (platinum). This electrode-PZT system is attached to a silicon wafer substrate (Figure 2). The PZT layer insulates the electrodes from each other, so that they act as a capacitor. An electric field is created when the electrodes are charged. This electric field causes the PZT layer to contract, deflecting the center of the electrode into the cylindrical hole in the silicon wafer below the top electrode. The larger the voltage applied between the electrodes the greater the electric field, causing a larger deflection.

By using a WYKO optical profiler, a white light interferometer, I was able to measure the height at various points on the microactuators. Measuring the difference in height between a reference point and the center of the microactuators, with 0V as a baseline, gives the deflection of the microactuators. Varying the voltage across the electrodes of the microactuators and measuring the deflection for each respectable voltage presents a plot-worthy relation of the microactuator deflection in respect to the voltage applied (Figure 3). Accurate control of the microactuator deflection will be needed throughout various applications; thus, the microactuator deflection must be

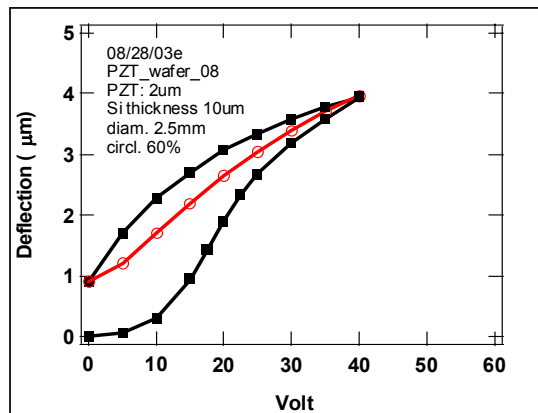


Figure 3: Deflection Profile of a microactuator, which is a plot of the deflection of the microactuator as the voltage varies. The black line starting at zero deflection is the start of the curve as the voltage increases up to 40V, then the voltage decreases to 0V on the other black line and back up to 40V on the red line.

characterized to determine the accuracy with which the microactuators can be deflected. The main goal of this project was to attain statistical data representing the deflection accuracy with numerous deflection curves for each type of microactuator.

Several deflection curves were attained during this project; however, many of the microactuators were failing at low voltages. These failures consisted of a reaction between the electrodes that eventually deteriorated the electrode-PZT system, similar to a dielectric breakdown between capacitors, yet at a low-voltage. The failure was attributed to poor PZT quality, yet it left the project in a standstill. This failure was not present in

one silicon wafer, leaving just one sample of reasonable microactuators to gain statistical data from. On the other hand, the failing microactuators were testable up to approximately 20 volts, yet this 20 volt limit significantly reduced the amount of deflection data attainable. Overall, the failure of the microactuators reduced the significance of the attainable results in this project.

The deflection curves I attained each have large deviations between some of the measurements that illustrates error associated with the interferometer measurements. Once statistical data is acquired from deflection curves, then this measurement error will have to be taken into account to ensure that the statistics of the microactuator accuracy don't also incorporate the measurement error. Accordingly, the project goal was changed since the significance of the microactuator statistical data was reduced due to the failure, and the measurement error need be analyzed and determined. The main project goal was changed to focus my work on the error analysis of the interferometer measurement process. Other goals for the project were developed. I was to test the microactuators to ensure that they endure the rapid periodic changes in displacement required. In addition, since the electrodes form a capacitor around the PZT thin film layer, I would attempt to study the change in charge on the capacitors, due to leaking current, over time.

There are several variables present in the interferometer measurement process. One must study and examine each variable to complete a proper error analysis. The major sources of potential error (variables) in the interferometer measurement process are: vibrations of the interferometer due to local vibrations in the table and due to air current in the lab, fluctuation in the voltage due to the power supply, deviation in the voltage magnitude due to the significant figures of accuracy in the voltmeter read-out, roughness (Ra) in the points being measured, and actual error in the WYKO measurement and WYKO software calculations.

Voltage fluctuations and deviation in the magnitude of the voltage were simple to determine. The largest change in displacement due to a 1 V change in potential throughout all of the deflection curves that I attain was 150nm. The voltage deviations were a maximum of 10 mV, so this would result in a maximum deviation in displacement of 1.5 nm between measurements, and a maximum deviation from the mean of 0.75 nm (7.5 Å). Overall, a deviation of 0.75 nm is insignificant in the data sets, and it is unobservable with the many other sources of error.

The possible error due to the voltage has been determined, and none of the other possible sources of error are dependent on the voltage. In an effort to simplify the error analysis, I was able to keep the voltage constant through numerous measurements in order to attain experimental distribution plots of the data acquired. Thus, these distribution plots are distributions of the remainder of sources of error. Before I go into depth about the distributions and the significance of each source of error, I will point out an interesting observation. The magnitudes of the displacements were consistent throughout the

numerous measurements when the voltage was held constant less than 3V; however, when the voltage was held constant above 3V, the magnitudes of the displacements would increase over time. This effect is due to piezoelectric creep, which is different from mechanical creep. Piezoelectric creep is repeatable and causes no damage to the piezoelectrics. Also, the change in displacement due to piezoelectric creep can be plotted as a log function, which fits the data sets I attained above 3V (Figure 4). Below 3V, the piezoelectric effect is nearly negligible so that the creep was unnoticeable within the distribution of data.

In addition, when the constant voltage applied from a voltage source is removed, there is a reversal of the piezoelectric creep effect. This reversal is of a lesser magnitude than the original creep, and it takes several hours to days for the displacement to maintain a constant value. Due to this reversal of piezoelectric creep, I was unable to attain values for the change in charge over time. Also, the presence of piezoelectric creep may make accurate actuation of the microactuators more difficult, which will have to be studied in future projects<sup>6</sup>.

Analyzing Gaussian distributions can reveal many interesting facts about a set of data; however, this analysis can be done with more than just Gaussian distributions. Gaussian distributions are the most common statistical model for sets of data, so they have

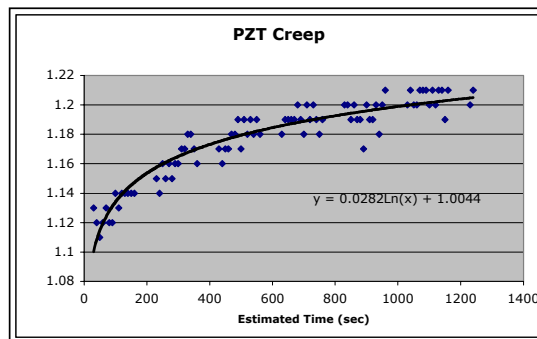


Figure 4: A log fit of the PZT creep on an acquired microactuator deflection data set at a constant voltage of 10V

standardized values that are known and evaluated throughout statistics. Other than the mechanical vibrations, the remainder of the sources of error can be statistically interpreted through Gaussian distributions. However, the mechanical vibrations can be assumed to be sinusoidal; thus, they should contribute a sinusoidal distribution factor to the final distribution of measurements made. The magnitude of the error due to vibrations was unknown, so I applied Gaussian statistics to the distributions and found that several did not fit into a Gaussian distribution.

The true magnitude of the sinusoidal factor can be determined merely through studying the distributions of data. On the other hand, a theoretical distribution of the data can be attained<sup>7</sup> that is dependent on the standard deviation of the Gaussian distribution factors, the amplitude of the vibrations on the interferometer, and on the distance between the reference point measured and the actuation point. Through the use of fringe counting on the interferometer, I estimated the amplitude of the vibrations on the interferometer. Using this amplitude, I fit the theoretical distribution with the statistical data sets (Figure 5), allowing me to obtain the standard deviation of the Gaussian distributed errors. I found the average standard deviation to be 7nm with a range of standard deviations within 2 nm of the 7nm mean. Further analysis demonstrated that the average error due to the vibrations alone is 56% with a standard deviation of 7nm.

Twenty microactuator cyclic tests were completed; in these tests the microactuators fluctuated through displacements at certain frequencies (with an alternating current) for an extended amount of time to observe their endurance to these circumstances. I completed 7 tests at 10Hz, 6 tests at 100Hz and 7 tests at 10kHz. Each of these tests were done with a 10V amplitude and for over one million cycles. Only one microactuator failed during the testing, and this was on a 10kHz test. The remainder of the tested microactuators showed no sign of wear or damage.

Theoretical Distribution Fit to an Experimental  
Distribution Data Set

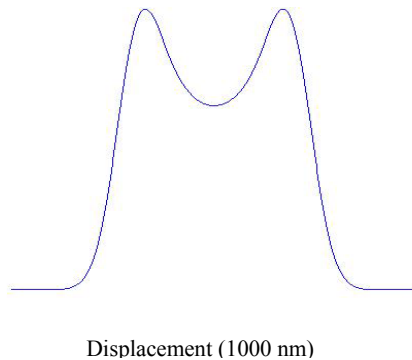


Figure 5: An Experimentally acquired microactuator deflection distribution fitted with the theoretical distribution

Overall, this project came to various conclusions. I found that the microactuators can withstand differing frequencies of alternating current. The piezoelectric creep deterred my efforts of attaining the change in charge over time results. The error associated with the voltage is nearly negligible, with a maximum error of 0.75 nm from the displayed

voltage. The vibrations on the interferometer cause an average error of 56%. The remaining 44% of error is due to the Gaussian sources of error, which have an average standard deviation of 7nm, with the range of the standard deviations being within 2nm of the 7nm mean.

I have several recommendations for future work with the thin film PZT microactuators. The microactuator failure needs to be investigated and negated for future microactuators to perform correctly. Deflection profiles, for statistical data, of the microactuators need to be gathered after the manufacturing of new non-faulty microactuators. Since the vibrations were the leading cause of error, then effort should be made to reduce the vibrations so that they contribute less error to the deflection profile statistics. Also, more cyclic tests need be done to ensure that the microactuators endure various amplitudes and ranges of frequencies. In order for the microactuators to be implemented into appropriate applications, projects will have to be done to determine how to accurately control their actuation with piezoelectric creep and hysteresis, which was not mentioned in this paper, accounted for<sup>6</sup>.

#### Extended Description

##### Voltage error:

Through the use of a voltmeter, the actual voltage difference between the two electrodes could be one half of the precision of the voltmeter below and one half of the same precision above the actual magnitude displayed on the voltmeter. The sum of these two deviations yields a maximum possible deviation, between two measurements, equal to the precision of the voltmeter. Choosing a voltmeter with the most precision could allow for the observation of voltage fluctuations, yet none were evident at a mV precision. A more complex analysis could be done on this system, yet an error of 10 mV (the precision above 5V on most voltmeters) would yield a negligible deviation of 0.75nm from the mean.

##### Change in charge over time:

The change in charge over time could not be measured with an ammeter since the current leakage in the wires used to measure the current would be much greater than that of the microactuator. An attempt to measure the change in charge over time was made through a different method. A deflection curve with respect to the voltage can be acquired for each actuator. Applying a voltage to the microactuator, disconnecting the voltage supply, and measuring the deflection with the WYKO optical profiler gives the initial conditions of the microactuator. Over time, the microactuator will lose deflection due to leaked

charge in the electrodes. This change in charge can inadvertently be determined by measuring the deflection after a period of time has elapsed. The deflection curve is known, so the change in voltage can be estimated from this curve since the voltage and deflection are known initially and the final deflection is known. For a capacitor, the voltage is equal to the charge over the capacitance of the capacitor. The capacitance can be estimated by permittivity of free space times the dielectric constant of PZT times the Area of the electrode and divided by the distance between the electrodes.

As mentioned in the text, the reverse piezoelectric effect takes several hours to days to complete. However, I made many measurements of this change in deflection with an elapsed time of one day for each measurement. Therefore, my measurements for the change in deflection also include the change due to creep, which is an unknown factor. Most of the change in deflection could be due to the creep, or the creep could be negligible. Due to a lack of time, I was unable to analyze this further, so I am left with no results for the change in charge over time.

## References

1. Hardy, J. W. Adaptive Optics: Technology developed during the cold war is giving new capabilities to ground-based astronomical telescopes. *Scientific American*. Unknown Journal Number, 60-65 (1994).
2. Tokovinin, A. Imaging through the turbulence. <http://www.ctio.noao.edu/~atokovin/tutorial/part1/turb.html> (2001)
3. Tokovinin, A. Correcting the turbulence: Deformable Mirrors. <http://www.ctio.noao.edu/~atokovin/tutorial/part2/dm.html> (2001)
4. Hishinuma, Y. & Yang, E. Piezoelectric Unimorph Microactuator Arrays for Single-Crystal Silicon Continuous Membrane Deformable Mirror. *IEEE/ASME Journal of Microelectromechanical Systems*, submitted (2005)
5. Mainland High School Piezo. <http://mainland.cctt.org/istf2003/piezo.asp> (2003)
6. Jung, H. Shim, J. Y. & Gweon, D. New open-loop actuating method of piezoelectric actuators for removing hysteresis and creep. *Review of Scientific Instruments*. 71, 3436-3440 (2000)
7. Levitt, J. A. & Stetson, K. A. Mechanical vibrations: mapping their phase with hologram interferometry. 15, 195-199 (1976)